ACS APPLIED NANO MATERIALS

www.acsanm.org Article

High Throughput Data-Driven Design of Laser-Crystallized 2D MoS_2 Chemical Sensors: A Demonstration for NO_2 Detection

Drake Austin, Paige Miesle, Deanna Sessions, Michael Motala, David C. Moore, Griffin Beyer, Adam Miesle, Andrew Sarangan, Amritanand Sebastian, Saptarshi Das, Anand B. Puthirath, Xiang Zhang, Jordan Hachtel, Pulickel M. Ajayan, Tyson Back, Peter R. Stevenson, Michael Brothers, Steve S. Kim, Philip Buskohl, Rahul Rao, Christopher Muratore,* and Nicholas R. Glavin*

Cite This: *ACS Appl. Nano Mater.* 2022, 5, 7549−7561 Read Online

ACCESS | Metrics & More | Article Recommendations | Supporting Information

ABSTRACT: High throughput characterization and processing techniques are becoming increasingly necessary to navigate multivariable, data-driven design challenges for sensors and electronic devices. For two-dimensional materials, device performance is highly dependent upon a vast array of material properties including the number of layers, lattice strain, carrier concentration, defect density, and grain structure. In this work, laser crystallization was used to locally pattern and transform hundreds of regions of amorphous MoS_2 thin films into 2D 2H-MoS_2. A high throughput Raman spectroscopy approach was subsequently used to assess the process-dependent structural and compositional variations for each illuminated region, yielding over 6000 distinct nonresonant, resonant, and polarized Raman spectra. The rapid generation of a comprehensive library of structural and compositional data elucidated important trends between structure−property processing relationships involving laser-crystallized MoS_2, including the relationships between grain size, grain orientation, and intrinsic strain. Moreover, extensive analysis of structure/property relationships allowed for intelligent design and evaluation of major contributions to device performance in MoS_2 chemical sensors. In particular, it is found that NO_2 sensor performance is strongly dependent on the orientation of the MoS_2 grains relative to the crystal plane.

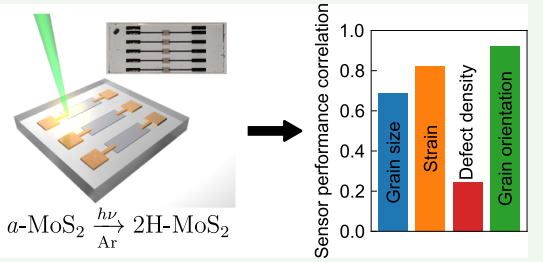

KEYWORDS: *molybdenum disulfide, few-layer, laser-induced crystallization, high-throughput characterization, Raman, UMAP*

INTRODUCTION

High throughput, data-driven design of nanomaterials is critical to ensure the rapid development of devices that operate across application areas including electronics, sensing, and optoelectronics. Relevant to sensor applications, two-dimensional (2D) transition metal dichalcogenides (TMDCs) exhibit exceptional electrical, optical, mechanical, and chemical properties with the benefit of having a high surface area-to-volume ratio. Dependent on the chemical composition and phase configuration,[1] TMDCs can present as semiconductors, semi-metals, and metals[2−4] and are comprised of covalently bonded layer sheets held together by weak van der Waals forces in the bulk form. The electrical and optical properties of TMDCs can be tuned by varying the number of layers,[5−7] applying strain,[8−11] and introducing dopants or defects.[12−16] Moreover, the high surface area-to-volume ratio, high electron mobility, and ease of functionalization make TMDC materials an ideal platform for the electronic detection of a multitude of liquid and vapor analytes.[17] In particular, NO_2 vapor remains one of the gold standards for evaluating 2D TMDC sensor performance, as the strong electron-withdrawing characteristics have been known to significantly modify the electronic and optical properties of TMDCs even at extremely low concentrations below 1 ppb.[17−19] Despite this, the understanding of material parameters dictating sensor performance is lacking as the variable space including grain size, thickness, strain, and doping are all expected to be strong contributors.

Data-driven design of electronic sensors is an attractive approach to efficiently and rapidly correlate multibody intrinsic material properties relevant to sensor performance optimization.[20] In the case of 2D MoS_2 chemical sensors, detection sensitivity is known to be non-monotonically responsive to the layer thickness,[21] grain size,[22−24] and defect density.[25,26] Moreover, 2D sensor devices are often fabricated from a finite batch of samples grown by wafer-scale, relatively uniform techniques including thermal decomposition, metal−organic chemical vapor deposition, or magnetron sputtering.[27−29]

Received: April 13, 2022
Accepted: April 27, 2022
Published: May 10, 2022

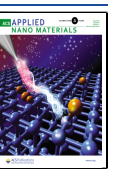

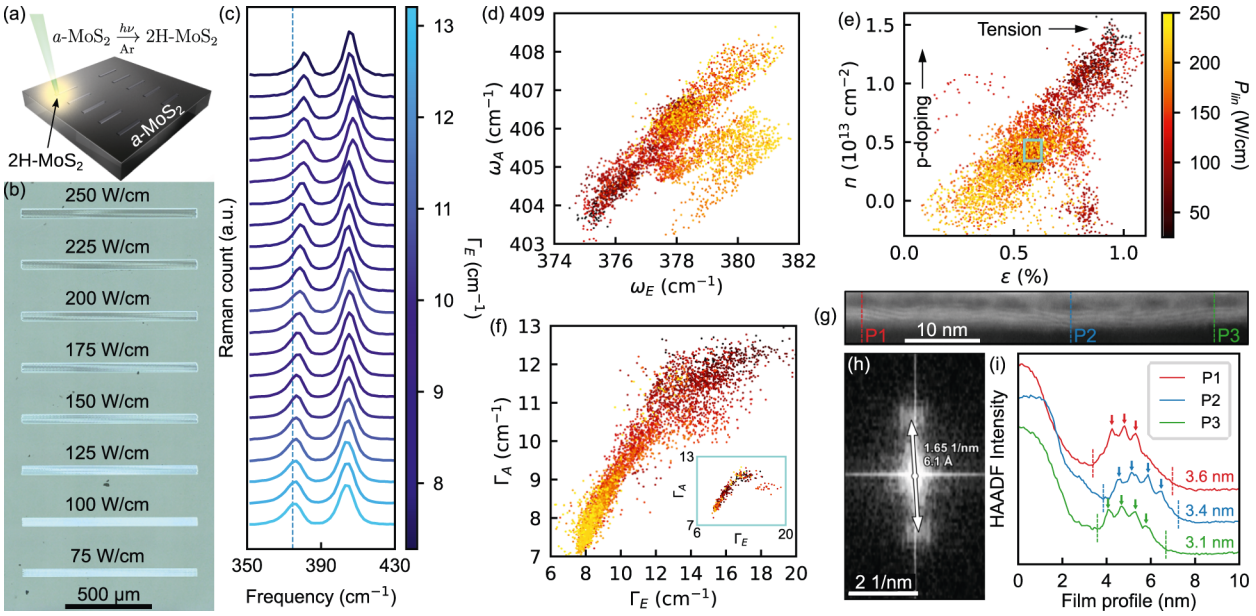

Figure 1. High-throughput analysis of Raman spectra in laser-crystallized 2H-MoS_2. (a) Schematic of laser processing with a 514.5 nm laser. (b) Optical image of laser-crystallized lines. (c) Waterfall plot of select 514.5 nm Raman spectra descending in order of decreasing E_{2g} frequency. The color scale indicates the E_{2g} fwhm. (d) Relationship between the A_{1g} and E_{2g} frequencies. The color scale indicates the linear power density used for annealing. The smaller clusters correspond to data points from the samples with the thinnest preannealed films (2.4 and 3.2 nm). (e) Strain and doping associated with the E_{2g} and A_{1g} frequencies. (f) Relationship between the A_{1g} and E_{2g} linewidths. A linear trend is observed for narrower linewidths that become nonlinear for broader linewidths. Inset: Same plot, but with the data set restricted to the strain and doping values indicated by the cyan box in (e). (g) STEM image of a 3.2 nm thick region annealed with P_{lin} = 125 W/cm and v = 1.0 mm/s. (h) FFT of the image in (g) showing interlayer spacing. (i) Plots corresponding to the profiles indicated in (g).

Following the growth process, annealing strategies such as thermal or photonic annealing can tailor the crystallinity, induce defects, or even manipulate electronic properties.[17,30,31] For films produced by such wafer-scale techniques, the tuning of these material properties must be done on a per-sample basis or must rely on film variation intrinsically present.[32] As a result, evaluating the relationships between the varying material properties is a time-consuming process. By introducing strategies to locally modify 2D materials after film growth, a large parameter space for material tuning can be achieved. For instance, exposure to ion beams has proven to be a viable technique to controllably introduce defects in TMDC films, allowing for the determination of the relationships between induced defects and the measured Raman and photoluminescence spectra.[13] Alternatively, laser patterning has been used to produce localized patterns within TMDC films through thermal decomposition[33] or thermally induced chemical reactions,[34] induce crystallization,[35−37] introduce or remove dopants and defects,[38−40] and induce structural changes.[41−43] However, the potential large-scale material variation associated with such techniques has revealed minimal connections to actual device applications such as chemical sensors.

To investigate the influence of such structure−property-processing relationships on the detection of NO_2 vapor, wafer-scale few-layer films of amorphous MoS_2 (a-MoS_2) were grown using magnetron sputtering, and localized regions were crystallized to 2H-MoS_2 through laser exposure. This investigation was broken into two parts. First, multiple samples with many laser-crystallized regions were fabricated for the purpose of characterization across a wide range of laser-processing conditions and their corresponding material properties. As the laser intensity and exposure time can be simply controlled, hundreds of micro-to-millimeter scale regions of crystallized MoS_2 can be patterned on a single sample at high throughput, each with varying material properties. From these conditions, thousands of individually unique Raman spectra across multiple samples were characterized to determine the relationship between strain, doping, out-of-plane orientation, defect density, and grain size as a function of our laser crystallization approach. Second, based on the structure−property-processing relationships uncovered from the aforementioned characterization, a smaller set of laser-processing conditions and material properties were used in the fabrication of MoS_2-based chemresistor sensor devices. From this high-throughput and data-driven approach, the interplay between intrinsic material properties and sensor device performance was evaluated upon exposure to NO_2 vapor at 1 ppm concentration. As such, critical design parameters were revealed for MoS_2-based sensors across different film thicknesses, grain sizes, grain orientations, intrinsic film strain, and degrees of p-type doping.

RESULTS AND DISCUSSION

Laser-Induced Crystallization of MoS_2 Thin-Films. Films of a-MoS_2 were grown on 0.5 mm thick Corning Eagle Glass substrates by pulsed DC magnetron sputtering at room temperature.[30,44] The magnetron sputtering technique is capable of producing samples with film thicknesses ranging from as few as four atomic layers to bulk films.[45] In this first part of the study, six samples were fabricated with film thicknesses of 2.4, 3.2, 3.6, 4.9, 6.5, and 7.8 nm. These amorphous samples were then exposed to a scanned, continuous-wave (CW) laser beam with a central wavelength of 514.5 nm. Laser exposure occurred while samples were immersed in an argon environment (Figure 1a) to reduce

https://doi.org/10.1021/acsanm.2c01614
ACS Appl. Nano Mater. 2022, 5, 7549−7561

reactions with ambient oxygen and moisture[46] as well as to provide an inert background pressure to minimize the formation of sulfur vacancies.[47] To produce uniform sample areas suitable for spectroscopic and electrical interrogation, the focused beam was raster-scanned eight times across the surface of the sample with a raster separation of 6 μm (center-to-center) over a length of 1 mm. Example confocal microscope images of the resulting laser-written lines are shown in Figure 1b (see Figure S1 for the full image). The laser was scanned over the surface with translation speeds of v = 0.1, 0.3, and 1.0 mm/s, and the range of laser power was selected from P = 25−300 mW. Independent control of these parameters resulted in localized control of the heating time and the peak temperature reached. In the case of CW lasers, the peak temperature is determined by the linear power density $P_{lin} = P/w$ independent of the focal spot size[48] where w is the $1/e^2$ focal spot radius.

High Throughput Characterization of Laser-Crystallized MoS_2. Raman spectroscopy was used as the primary method of characterization as its high spatial resolution (1 μm) allowed for the acquisition of many spectra within every laser-crystallized region. A total of 4529 unpolarized Raman spectra using a 514.5 nm excitation laser were acquired within localized crystalline regions across samples of six different film thicknesses (2.4, 3.2, 3.6, 4.9, 6.5, and 7.8 nm). This large number of spectra was acquired by scanning the Raman laser over the width of each laser-written line, resolving the spatial variation in the Raman signal due to the annealing laser's Gaussian focal spot profile (Figure S2).

The values of the peak intensity I_i, frequency ω_i, and linewidth Γ_i (as determined by the full width at half maximum (fwhm)) of the E_{2g} and A_{1g} peaks (i = E and A, respectively) were extracted for each spectrum by fitting to two pseudo-Voigt functions with the initial guesses determined automatically using peak-finding software (additional details found in Supporting Information including example fits in Figure S3). The data was filtered to remove spectra with E_{2g} peak intensities in the bottom 5th percentile of each laser-written line. This was done in order to exclude particularly weak Raman signals, that is, the peripheries of the laser-written lines. Examples of the normalized spectra are shown in a waterfall plot in Figure 1c where the stacking order is determined by the extracted E_{2g} frequency and the color scale is determined by the extracted E_{2g} fwhm linewidth.

Using this data, the key relationships observed between the extracted fitting parameters and the physical characteristics with which they correspond can be analyzed across all film thicknesses. The extracted frequencies of the A_{1g} and E_{2g} Raman peaks (ω_A and ω_E) of over 4500 unique spectra are shown in Figure 1d, where the color scale indicates the linear power density of the annealing laser (P_{lin}). Three linear trends are observed, with higher values of P_{lin} tending to result in crystallites with higher peak frequencies for both E_{2g} and A_{1g} Raman modes. The smaller linear regions offset from the main trend correspond specifically to the thinnest amorphous films with a preannealed thicknesses of 2.4 and 3.2 nm (see Figure S5a for the same plot with these data points excluded), suggesting that the mechanisms responsible for the frequency shifts are influenced by the number of molecular layers for thinner films. While film thickness can influence peak frequencies by red-shifting the A_{1g} peak and blue-shifting the E_{2g} peak with increasing thickness,[6,8] the frequencies will be within 0.5 cm^{-1} of bulk values when the film thickness reaches five molecular layers.[7] This suggests that variations in the film thickness alone cannot account for the observed frequency shifts. However, strain and doping are also known to influence the frequencies of these peaks.[8,9,32,49,50] While the samples here were not externally strained during analysis, internal in-plane and out-of-plane strain may still be present due to lattice mismatches between grains. The frequency shift $\Delta\omega$ can be related to strain and doping within the material through the following expression[49]

$$\Delta\omega_i = -2\gamma_i\omega_i^0\varepsilon + k_{n,i}n \quad (1)$$

where γ is the Grüneisen parameter, ω^0 is the frequency corresponding to undoped and unstrained MoS_2, ε is the amount of strain, k_n is an empirical constant, n is the carrier concentration (negative for electrons and positive for holes), and the subscript i = E, A indicates that the value corresponds to either the E_{2g} or A_{1g} peak. The first term describes how changes in the volume of the lattice influence its in-plane and out-of-plane vibrational properties (the E_{2g} and A_{1g} Raman modes, respectively). The second term describes an empirically observed, quasi-linear relationship for MoS_2.[50] Equation 1, therefore, provides a one-to-one mapping between the peak frequencies and the amount of strain and doping present in the film. It is worth emphasizing, however, that the acquired Raman signals represent an average over the areas irradiated by the excitation laser. While the strain and doping values extracted from eq 1 for a single-crystal, monolayer film could more reliably be treated as uniform over the irradiated area, the values extracted for a polycrystalline, multilayer film instead represent average values over the individual layers throughout the thickness of the film and the ensemble of single-crystal grains comprising the irradiated region. Additionally, the frequency shifts in a multilayer film must be assumed to remain linear with strain and doping in order for eq 1 to apply.

With these points in mind, the appropriate empirical constants in eq 1 must be estimated. The values for ω^0 are dependent on film thickness and are estimated based on the values reported by Li et al.[51] However, multilayer values for γ and k_n have not been reported to the best of the authors' knowledge. Using the monolayer MoS_2 values for γ and k_n instead,[49] the amount of strain and doping can be extracted from the peak frequencies in Figure 1d and are shown in Figure 1e. Overall, it is found that the primary charge carriers are holes and the crystal grains are under tension. As few-layer films were used in this study, the appropriate values for γ and k_n may differ from those of monolayer films, and so the absolute values of the strain and carrier concentration are only an estimate of quantitative values. However, the relative differences between data points can still be compared. Again, a linear trend is observed, though the data points from the 2.4 and 3.2 nm thick films largely follow the same linear trend as the thicker films. Equation 1 provides a plausible explanation for this: the values for ω^0 are dependent on the number of molecular layers up until approximately four layers, after which the film can be treated as bulk-like when considering these values. Additionally, the values for γ and k_n likely do not vary considerably over the range of film thicknesses studied here. Otherwise, the data points corresponding to each film thickness would appear in disparate regions of Figure 1e, as they do for the thinner films in Figure 1d. Overall, it is found that less-doped regions tend to be under less strain, with the least amount of doping and strain corresponding to the regions

https://doi.org/10.1021/acsanm.2c01614
ACS Appl. Nano Mater. 2022, 5, 7549−7561

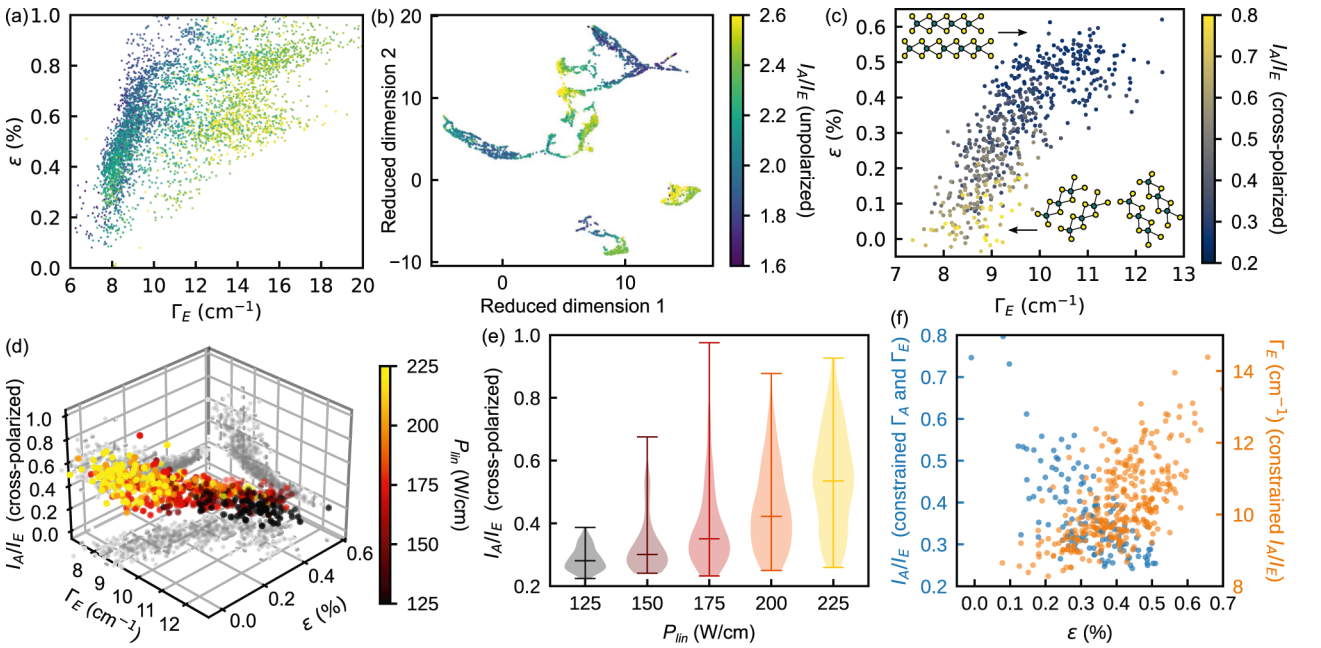

Figure 2. Analysis of polarized Raman spectra. (a) Relationship between the strain and the E_{2g} fwhm linewidth with the color scale indicating the A_{1g}/E_{2g} peak intensity ratio. A linear region is observed for narrower linewidths, which also corresponds to points with smaller A_{1g}/E_{2g} peak intensity ratios. (b) UMAP plot representing a dimensional reduction of all 514.5 nm Raman spectra into a 2D plane (see Supporting Information for details). Each point represents a particular Raman spectrum. The color scale indicates the A_{1g}/E_{2g} peak intensity ratio. (c) Same as (a), but under 514.5 nm cross-polarized Raman spectroscopy for the 3.4 nm film. Higher frequencies are observed, likely due to oxidation of the sample since its original characterization under unpolarized Raman spectroscopy. Inset images illustrate grain orientation for high and low A_{1g}/E_{2g} peak intensity ratios. (d) 3D plot with 2D projections showing the relationships between the A_{1g}/E_{2g} peak intensity ratio and the E_{2g} fwhm and strain. The color scale indicates the linear power density. (e) Violin plot showing the distribution of A_{1g}/E_{2g} peak intensity ratios for each linear power density used. (f) Plot of the A_{1g}/E_{2g} peak intensity ratio and E_{2g} fwhm versus strain. For the A_{1g}/E_{2g} peak intensity ratio, the data set is constrained such that 8.9 $cm^{-1} < \Gamma_E < 9.8$ and 8.7 $cm^{-1} < \Gamma_A < 9.7$ cm^{-1}. For the E_{2g} fwhm, the data set is constrained such that $0.27 < I_A/I_E < 0.35$.

annealed with the largest laser intensity corresponding to the highest localized temperatures.

The influence of annealing temperature on strain can be further analyzed by considering the linewidth of the Raman peaks for MoS_2[52] (Γ_A and Γ_E), shown in Figure 1f. Similar to Figure 1e, which relates strain to doping, a roughly linear trend is observed when comparing the linewidths Γ_A and Γ_E. This is expected as the E_{2g} and A_{1g} peak linewidths correspond to disorder (i.e., grain size) in the lateral and transverse directions, respectively,[53] with smaller linewidths corresponding to less disorder (larger grains). It can be seen that higher annealing temperatures tend to result in larger grains, which offers an explanation for the observed trend in the strain. With increasing lateral disorder, each individual crystallite exerts a greater force on its neighbors at the grain boundary due to the mismatch in their crystallographic order. This results in more overall strain, which is reduced as the grain size increases and the number of grain boundaries decreases.[54] At the largest linewidths, a deviation from linearity is observed, possibly due to changes in doping and strain.[49] This can be examined by restricting the data set to a small range of nearly constant strain and doping values, indicated by the data points within the cyan box in Figure 1e. This range of values was chosen by selecting the highest-populated bin within the strain and doping data. The resulting plot of this restricted data set is shown in the inset of Figure 1f. The linear trend is still observed for smaller linewidths but eventually levels off for the A_{1g} peak, suggesting that strain and doping are not the cause of the observed nonlinearity. Instead, it is proposed here that, while the amount of lateral disorder (Γ_E) can continue to increase, the amount of transverse disorder (Γ_A) is limited by the finite film thickness. To observe the extent of atomic disorder for a typical annealed region, scanning transmission electron microscopy (STEM) was used to image the 3.2 nm thick sample annealed at conditions favorable for high crystalline order (Γ_E = 11.2 ± 1.7 cm^{-1}, Γ_A = 10.3 ± 0.4 cm^{-1}). The resulting STEM image, its fast Fourier transform (FFT), and select line profiles are shown in Figure 1g–i. The annealed film is 3–4 molecular layers thick (~3.4 nm) with a grain size of roughly 10 nm with most of the crystallites oriented in-plane.

In order to investigate the interplay between strain/doping and crystal grain size, the strain and linewidth values extracted from the library of spectra collected from the samples are shown in Figure 2a. In this case, a linear trend is observed for Γ_E values below approximately 10 cm^{-1}. Beyond this, the strain values level off while also broadening significantly. In order to further elucidate this trend, the data points were colored based on the values of the A_{1g}/E_{2g} peak intensity ratio (I_A/I_E) from the unpolarized spectra. The linear and nonlinear regions of the plot are visibly separated based on these values, which are known to relate to the Raman excitation laser polarization and the grain orientation.[6,55]

Utilizing the large available data set, further analysis was performed using uniform manifold approximation and projection (UMAP), a dimension reduction technique useful for visualizing multidimensional data sets.[56] UMAP is a nonlinear reduction technique that preserves local and global data structures based on pairwise probabilities. This probabilistic approach differs from linear reduction techniques, such as principal component analysis (PCA),[57,58] which are better

https://doi.org/10.1021/acsanm.2c01614
ACS Appl. Nano Mater. 2022, 5, 7549–7561

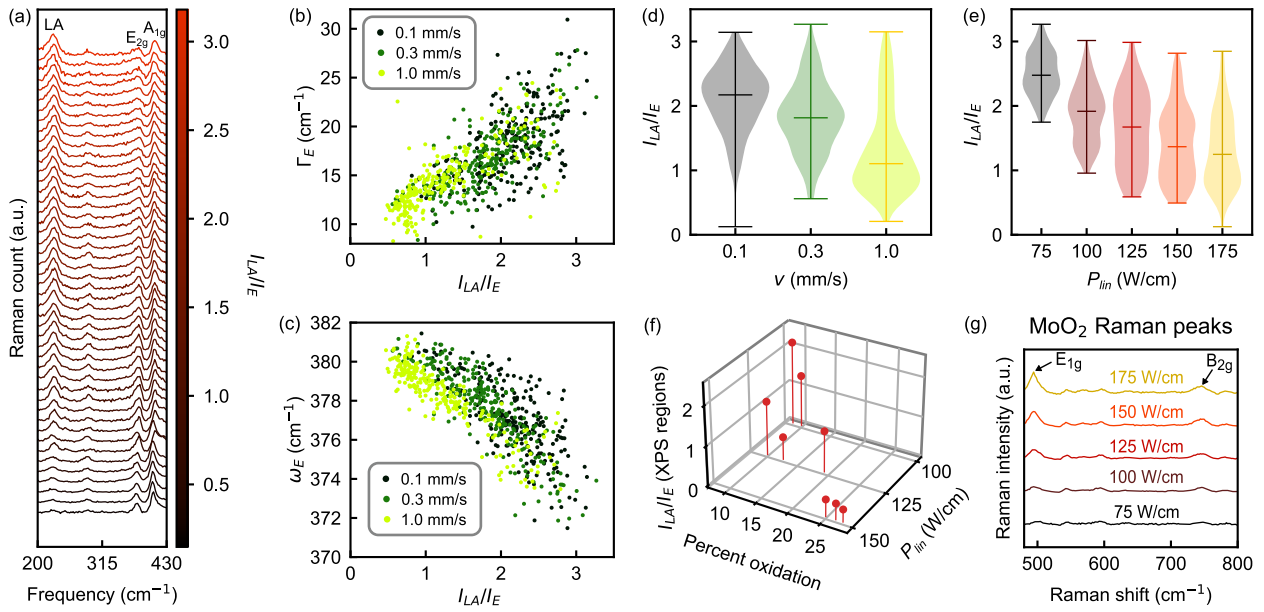

Figure 3. Analysis of resonant Raman spectra. (a) Waterfall plot of select resonant Raman spectra (3.6 nm film only), stacked and colored based on the LA/E_{2g} intensity ratio. (b,c) Plots of the E_{2g} linewidth and frequency vs the LA/E_{2g} intensity ratio. The color scale indicates the speed of the translation stage during laser annealing. (d,e) Violin plots of the LA/E_{2g} peak intensity ratio for each v and P_{lin} value. (f) 3D plot of the LA/E_{2g} peak intensity ratio vs percent oxidation and P_{lin} for 1 mm^2 regions formed by raster-scanning the laser at P_{lin} = 100, 125, and 150 W/cm and v = 0.1, 0.3, and 1.0 mm/s. The percent oxidation was determined by acquiring and fitting X-ray photoelectron spectroscopy (XPS) spectra of each region and extracting the relative intensity of the Mo 3d(+6, Mo_xO_y) peak. (g) Nonresonant Raman spectra for v = 1 mm/s regions showing E_{1g} and B_{2g} peaks characteristic of MoO_2. Each spectrum represents the median value of all spectra across the width of each raster-scanned region and is normalized to the intensity of the 2H-MoS_2 A_{1g} peak.

suited for multicolinear high dimensional data as they reduce data through a linear change of basis. While PCA is suited for capturing variance in the global data through linear transforms, UMAP is well-suited for identifying continuous trends by preserving global relationships while also maintaining neighborhoods of similar data—see Supporting Information for a detailed mathematical description of the technique. Applying UMAP to the data set of nonresonant Raman spectra within a frequency range of 325−466 cm^{-1} (i.e., a range containing the E_{2g} and A_{1g} peaks) results in Figure 2b. Within this plot, each data point represents a single Raman spectrum, as indicated by the inset. The horizontal and vertical axes represent the reduced dimensions onto which the high-dimensional data set has been projected and do not have a simple physical interpretation. However, distances between points within this plot do have an intuitive interpretation: they represent how similar each point (Raman spectrum) is probabilistically across all relevant features of the spectra (see Figure S8 for an illustration of this). By coloring each point based on the value of the corresponding fitting parameters and relationships between them (e.g., I_A/I_E in Figure 2b), potential trends can be identified. Here, Figure 2b shows significant clustering based on I_A/I_E, indicating that points with similar I_A/I_E ratios tend to also be similar in other aspects of their Raman spectra. This suggests a potential relationship between grain orientation and other critical variables.

As previously mentioned, I_A/I_E is influenced by the Raman laser polarization in addition to the grain orientation. This is because the light emitted by these two modes is polarized (linear for A_{1g}, elliptical for E_{2g}),[55] causing I_A/I_E ratios to vary based on the orientation of the grains with respect to incident laser light as well as the Raman setup itself. The latter effect can be mitigated by using polarized Raman spectroscopy, which makes use of a polarizer to only analyze components of the Raman signal that are crossed (or parallel) to the polarization of the Raman excitation laser. With a cross-polarized setup, the A_{1g} signal is suppressed for crystallites oriented in-plane. Consequently, small values of I_A/I_E indicate that the crystal grains are oriented in-plane, while larger values of I_A/I_E indicate that the crystal grains are oriented at an angle relative to the crystal plane. Polarized Raman data were therefore collected to further investigate the trends revealed in Figure 2a,b. This was done in the same fashion as in the unpolarized case, but using a single film thickness for simplicity, resulting in over 900 unique polarized Raman spectra. For this purpose, the 3.2 nm thick film was used, as it showed the clearest linear trend (Figure S6). For each Raman scan across the width of each line, both cross- and parallel-polarized configurations were used (commonly denoted as $zXY\bar{z}$ and $zXX\bar{z}$, respectively). The resulting strain and Γ_E values for the cross-polarized case are plotted in Figure 2c with the color scale indicating the cross-polarized I_A/I_E ratio. A 3D plot of all three variables is also shown in Figure 2d with 2D projections along each axis and the color scale indicating the linear power density. These variables serve as proxies to the structural properties of the lattice, namely: grain size (higher Γ_E, smaller grain size) and grain orientation (higher I_A/I_E, larger angle relative to the crystal plane). It is worth emphasizing here that, as the spatial resolution of the Raman spectra is 1 μm, the measured values constitute averages over many crystal grains. Overall, higher I_A/I_E ratios are observed at lower strain values and lower Γ_E values. This suggests that out-of-plane oriented (OoPO) grains tend to be larger (lower Γ_E) and under less strain. While it is difficult to causally link any two variables, it is likely that OoPO grains are forming due to

https://doi.org/10.1021/acsanm.2c01614
ACS Appl. Nano Mater. 2022, 5, 7549−7561

the higher annealing temperatures, which also naturally tends to result in larger grains and less strain, as discussed earlier. This is supported by Figure 2e, which shows a violin plot of I_A/I_E as a function of the linear power density. Lower annealing temperatures tend to result in lower ratios with a smaller variance, corresponding to a large number of in-plane-oriented (IPO) grains. In contrast, higher annealing temperatures show larger ratios with a larger variance, corresponding to increased populations of both OoPO and IPO grains.

From these trends, the source of the variation in strain can be further investigated. As previously discussed, lattice mismatches at grain boundaries can result in strain, with smaller grain sizes corresponding to a higher density of grain boundaries and therefore more strain. It is also possible that the grain orientation influences the amount of strain in the crystal plane, with IPO grains experiencing more strain due to lattice mismatch from neighboring grains on all sides. Utilizing the large number of data points available, both effects can be evaluated by constraining the data set, as shown in Figure 2f. In this plot, the blue data points correspond to I_A/I_E values where Γ_A and Γ_E have been restricted to ranges 8.9 $cm^{-1} < \Gamma_E < 9.8$ and 8.7 $cm^{-1} < \Gamma_A < 9.7$ cm^{-1}, limiting the effect of grain size on any observed trends. Similarly, the orange data points correspond to Γ_E values, where I_A/I_E has been restricted to the range $0.27 < I_A/I_E < 0.35$, limiting the effect of grain orientation. In both cases, clear correlations remain, supporting the claim that the observed strain is caused by lattice mismatches between neighboring grains, with smaller grain sizes (larger Γ_A and Γ_E) leading to more strain and OoPO grains (larger I_A/I_E) partly relieving this strain.

Another key contribution to sensor performance is the extent of defects within the lattice structure.[25,26] To qualitatively assess this, unpolarized, resonant Raman spectra using a 633 nm excitation laser were collected for the 3.6 nm film. When excited with an excitation wavelength close to the direct band gap of MoS_2, a nonzone center and combination modes emerge that are not observed in nonresonant Raman spectra (i.e., with 514.5 nm excitation). The emergence of a low-frequency longitudinal acoustic (LA) mode centered at 225 cm^{-1} corresponds to the scattering of LA phonons at the M point in the Brillouin zone and has been shown to be directly tied to lattice disorder or defect density.[53,59,60] Example resonant Raman spectra are shown in a waterfall plot in Figure 3a, where the stacking order and color scale correspond to the LA/E_{2g} peak intensity ratio (I_{LA}/I_E). These spectra were each fitted in the same manner as the nonresonant Raman spectra but with an additional peak to account for the LA mode. As the peaks corresponding to the A_{1g} and E_{2g} modes each contain an additional peak under resonant excitation that has not been accounted for here for simplicity, the extracted fitting parameters for these modes cannot be considered as accurate as those determined from nonresonant excitation. Nevertheless, the general trends between each parameter can still be considered—for example, a higher I_{LA}/I_E ratio will correspond to more lattice disorder for a given crystal size. Plotting Γ_E and ω_E versus I_{LA}/I_E (Figure 3b,c) shows a clear trend where regions with smaller grains (higher Γ_E) and more strain (lower ω_E) tend to have greater defect densities. Coloring each data point based on the translation speed of the sample under laser exposure reveals a clustering based on speed, indicating that the laser processing conditions can directly control defect density. By generating a violin plot of I_{LA}/I_E for each speed (Figure 3d), a decreasing trend is observed, where regions annealed at slower speeds (i.e., heated for longer times) tend to be more defective. In contrast, higher P_{lin} values show lower I_{LA}/I_E ratios (Figure 3e), suggesting that higher annealing temperatures lead to less defective films.

Raman spectroscopy alone, however, is not sufficient to determine the type of defects present. In particular, it is expected that the laser-annealing process could potentially result in oxidation due to the presence of residual oxygen in the argon environment. Such oxidation could result in oxygen dopants acting as substitutional defects. By performing XPS, the degree of oxidation was determined. This was performed on 1 mm^2 regions (corresponding to twice the XPS spot size) formed on the same 3.6 nm sample used previously by raster-scanning the laser at various critical conditions determined through the initial screening of the Raman data mentioned above. The percent oxidation was determined by fitting the resulting spectra and extracting the intensities of the relevant peaks (see Supporting Information for details). Before undergoing XPS analysis, the I_{LA}/I_E ratio of each region was characterized with resonant Raman spectroscopy in the same manner as the previous laser-annealed regions. Figure 3f shows the resulting 3D plot of the I_{LA}/I_E ratio vs the percent oxidation and P_{lin}, where this ratio is found to decrease with the degree of oxidation. The I_{LA}/I_E ratio for these XPS regions is also found to decrease with increasing values of P_{lin}, consistent with the results from the larger data set in Figure 3e. Altogether, higher annealing temperatures are found to simultaneously result in both more oxygen and fewer defects. This suggests that the oxygen present in the regions annealed at lower temperatures acts as a substitutional defect, while much of the oxygen present in the regions annealed at higher temperatures does not. It is proposed here that, at higher annealing temperatures, the MoS_2 reacts with oxygen to form Mo_xO_y crystallites. Oxygen atoms within these crystallites no longer act as defects within the MoS_2 lattice, and the I_{LA}/I_E is consequently found to decrease. This also offers an explanation for the source of doping as well as the relationship observed in Figure 1e between the carrier density and P_{lin}: regions that were annealed at lower temperatures show a higher degree of p-doping due to the presence of oxygen dopants. However, as P_{lin} increases, the density of oxygen dopants decreases as they become locked away in Mo_xO_y crystallite bonds, resulting in regions that are less p-doped. This hypothesis can be confirmed by analyzing the nonresonant Raman spectra at higher frequencies where characteristic Mo_xO_y peaks can be found. Figure 3g shows the spectra of the 3.6 nm sample for each value of P_{lin} with the scan speed fixed at v = 1 mm/s. These spectra are the median values across the width of each raster-scanned region, normalized to the intensity of the 2H-MoS_2 A_{1g} peak. Peaks characteristic of MoO_2 are apparent, most notably the E_{1g} and B_{2g} peaks. These peaks are found to increase with P_{lin}, indicating that MoO_2 crystallites are forming more readily at higher annealing temperatures. These results also offer a potential explanation for the decrease in the I_{LA}/I_E ratio with increasing scan speed: as observed in a previous study of laser-annealed 2H-MoS_2.[45] MoO_2 is a reaction intermediate that forms most readily at higher scan speeds (shorter heating times) when formed through laser-annealing and begins oxidizing further at slower scan speeds (longer heating times). However, it is not clear why crystalline MoO_3 does not form at these scan speeds (no characteristic MoO_3 Raman peaks are observed for any region); further studies

https://doi.org/10.1021/acsanm.2c01614
ACS Appl. Nano Mater. 2022, 5, 7549−7561

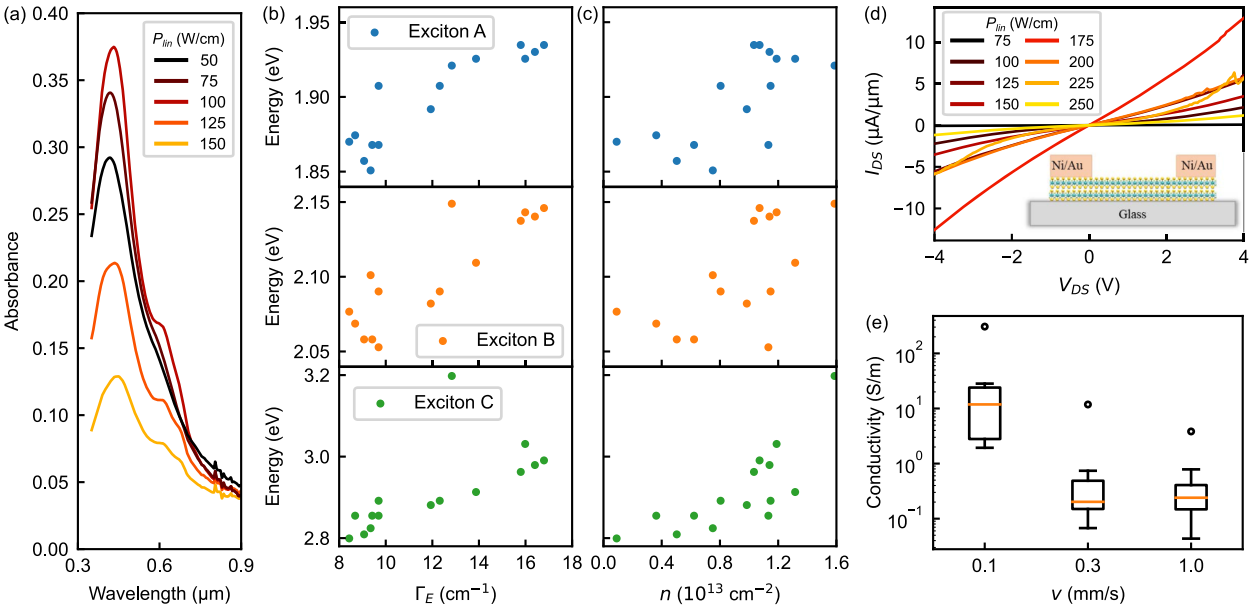

Figure 4. Optical and electrical characterization. (a) Absorbance spectra for select regions of the 7.8 nm film. (b) Exciton energies vs E_{2g} fwhm linewidth. (c) Exciton energies vs the Raman-derived carrier concentration. (d) *IV*-curves for each selected region of the 3.6 nm film. Inset: diagram illustrating the geometry of the measurement setup. (e) Boxplot of the resulting conductivity vs scan speed.

covering few-layer 2H-MoS_2 properties over a wider range of scan speeds are needed.

Finally, it is also worth noting that the majority of oxygen dopants present in the regions annealed at lower temperatures were not introduced during the laser-annealing process. This is evidenced by the 11% oxidation measured for the precursor film, which is comparable to the 9−12% oxidation measured for regions annealed at P_{lin} = 100 W/cm. Instead of introducing additional oxygen, lower annealing temperatures primarily redistribute extant oxygen atoms into the crystalline structure.

High Throughput Evaluation of Electronic and Optical Characteristics. Further characteristic information about each laser-annealed region can be determined by complementary optical and electrical measurements. For optical absorbance measurements, the sample with the largest preannealed film thickness (7.8 nm) was chosen as it exhibits the greatest optical density for intensity-dependent optical characterization. Representative absorbance spectra are shown in Figure 4a as a function of increasing power involving laser crystallization. Note that the measured absorbance spectra constitute ensemble responses for each annealed region (spatial resolution limit of approximately 55 μm^2), rather than capturing the variation within each region as in the case of Raman spectroscopy. Although this limits the number of spatially resolved optical data points, a comparison to the Raman data was performed by calculating the median value of each extracted Raman spectra parameter (i.e., $\Gamma_{E,A}$, $\omega_{E,A}$, $I_{E,A}$, ε, and n). In this way, the ensemble optical intensity responses can be correlated to the higher resolution Raman characteristics.

From the absorbance spectra, the associated A, B, and C exciton energies for MoS_2 can be related to predicted or known structural characteristics. For prototypical semiconducting 2H-MoS_2, the A and B excitons correspond to the energy gap between the conduction band minimum and the two valence band maxima associated with the spin−orbit split valence bands.[61] Additionally, the C exciton corresponds to a region in the band structure where the valence and conduction bands are nearly parallel, leading to band-nesting and strong absorption.[61] Characterizing peak exciton energies can subsequently yield information about the band structure within the 2H-MoS_2 laser-crystallized region of interest. The C exciton energies for MoS_2 were extracted from the primary peak in the absorbance spectra; however, as this peak dominates the absorbance, the A and B exciton peaks are less apparent and can present as changes in the slope rather than as true peaks. The energies for these excitons are therefore extracted from the associated peaks in the derivatives of the absorbance spectra (see Supporting Information for details). Across the laser-crystallized regions, a blue shift in the exciton energies is observed (∼0.08 eV for the A and B excitons and ∼0.19 eV for the C exciton) relative to the E_{2g} linewidth (Figure 4b). This suggests that regions with smaller grains tend to have a wider band gap between the valence and conduction bands, particularly near the band-nesting region. Wendumu et al.[62] theoretically investigated the influence of nanocluster (i.e., <10 nm) MoS_2 lateral grain sizes and showed that there is an intrinsic interplay between edge metallic properties and inner semiconducting properties as a function of flake (or grain) size. Similar size-dependent spectral features have also been observed for nanocluster MoS_2 in solution.[63] Huang et al.[10] show that—in the case of monolayer 2H-MoS_2—the strain induced by an increase in the number of grain boundaries (presumably resulting in smaller grain sizes) may lead to a decrease in the band gap. However, the amount of tensile strain investigated by Huang et al. (up to ∼6%) is significantly greater than that observed here (up to ∼1%). The results here instead suggest that the changes in exciton peak energy appear more strongly correlated to changes in the carrier concentration. This is supported by Rao et al.[64] and Stevenson et al.[16] who observed a blue shift in the energy of the A exciton emission and complex refractive index peak dispersions, respectively, upon passivation of sulfur vacancies with oxygen (i.e., when the material becomes less n-type due to a reduction in the electron density). Plotting the exciton energies vs the

https://doi.org/10.1021/acsanm.2c01614
ACS Appl. Nano Mater. 2022, 5, 7549−7561

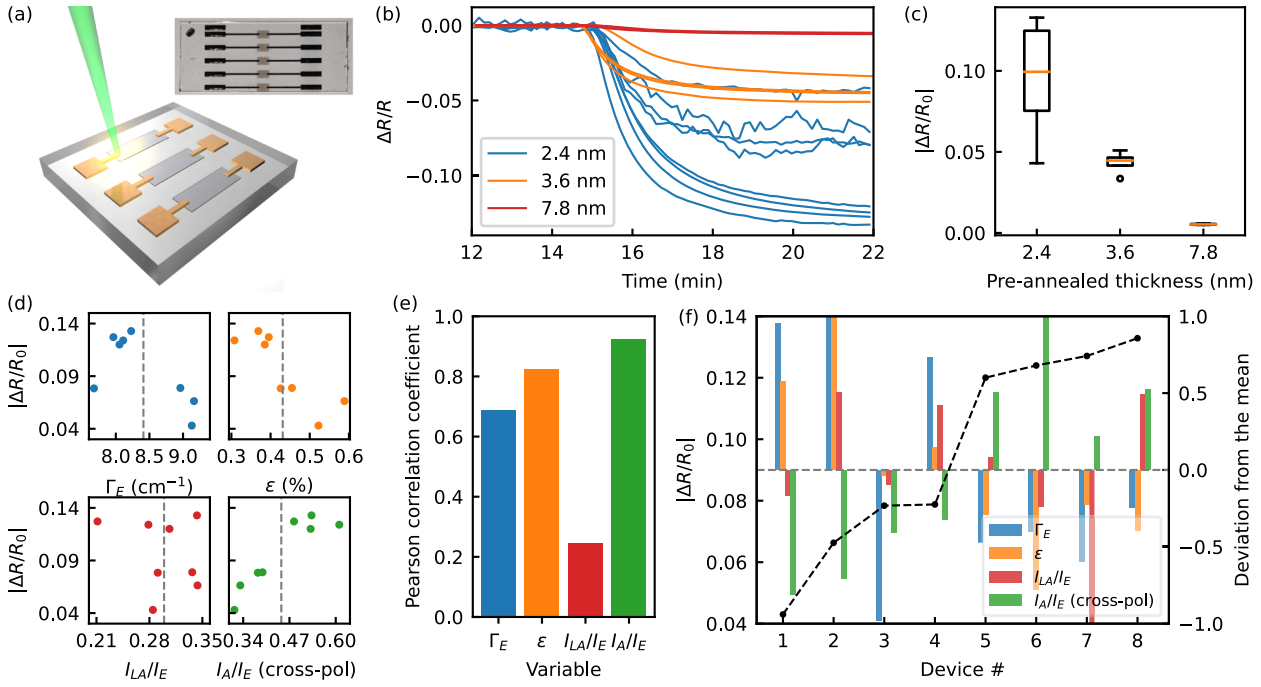

Figure 5. Gas sensor testing and analysis. (a) Schematic illustrating the geometry of the sensors: a sensing region (laser-annealed 2H-MoS_2) between two gold contacts. Inset: an image of a sensor with the a-MoS_2 film clearly visible between contacts. (b) Plot of the sensor response (relative change in resistance) to 1 ppm of NO_2 for each device as a function of time, with the color indicating the film thickness used for the device. (c) Boxplot of the sensor response for each film thickness. (d) Plot of the sensor response vs the E_{2g} linewidth, strain, LA/E_{2g} intensity ratio, and the (cross-polarized) A_{1g}/E_{2g} peak intensity ratio. The grey dashed lines correspond to the mean values of each Raman parameter. (e) Bar plot of the Pearson correlation coefficients associated with the plots in (d). (f) Plot of the sensor response of each device overlaid on top of a histogram of the parameters used in (d). Dashed grey line represents the mean value of each Raman parameter, and the height of the bars represents the deviation from the mean relative to the maximum deviation.

carrier concentration (Figure 4c) shows a similar blue shift when the material becomes more p-type due to the presence of oxygen dopants discussed previously.

Electrical conductivity measurements were also carried out for the film with a 3.6 nm preannealed film thickness at various conditions. The resulting *IV*-curves from select regions are shown in Figure 4d. Together with the film thickness, the conductivity can be calculated, which represents an averaging over the width of each annealed region. Generating a box plot of the conductivities for each scan speed results in Figure 4e, showing significantly higher conductivities for the regions annealed at slower speeds. As previously discussed, regions annealed at slower speeds tend to result in a more defective film (Figure 3b) due to the presence of oxygen dopants. At higher annealing speeds, the defect density decreases, leading to a corresponding decrease in conductivity.

Data-Driven Optimization of Thin-Film Chemical Sensors. Thin films of crystalline MoS_2 show significant promise for being used in electronic chemical sensing devices,[17,65,66] where modulations of the carrier density are done by binding a molecule to the surface, modifying the electrical conductivity within the channel. As the laser-crystallization approach described in this work highlights access to a broad range of grain sizes, defect densities, strain, carrier concentrations, and grain orientations, chemical sensors were fabricated using selected conditions to evaluate their relationship to sensitivity and limit of detection. For this second part of the study, select conditions from the analysis performed in Figures 1−4 were executed on samples with film thicknesses of 2.4, 3.6, and 7.8 nm to form sensor devices. These sensor devices were made by first fabricating multiplexed Cr/Au contacts onto a glass substrate with a channel gap with dimensions of 200 μm^2. Amorphous MoS_2 was then deposited over the channel gaps for each device by using a mask with 1.4 mm × 0.9 mm rectangular holes. The channel gaps for each sample were annealed by raster-scanning the laser with different linear power densities and scan speeds (Figure 5a), producing sensing regions with a wide range of material properties. The sensing regions were then characterized by acquiring multiple Raman spectra over the width of each region using unpolarized, polarized, and resonant Raman. As was done previously, the peak intensities, linewidths, and frequencies were determined by fitting the spectra, which could then be used as proxies for material properties of interest. In particular, the E_{2g} linewidth (from unpolarized Raman), the LA/E_{2g} peak intensity ratio (from resonant Raman), and the A_{1g}/E_{2g} peak intensity ratio (from cross-polarized Raman) were chosen as correlates to grain size, defect density, and grain orientation, respectively, while strain was calculated using eq 1. Given that the sensor response is based on the average material properties of the sensing region, the median values of these Raman parameters for each device were used throughout this analysis.

To determine the sensing response of each of these regions, the relative change in resistance ($\Delta R/R$) across 15 unique devices was monitored over time during exposure to 1 ppm of NO_2 with the resulting responses shown in Figure 5b. A strong dependence on the film thickness on overall sensitivity (i.e., the largest value of $\Delta R/R$) was observed and is further illustrated in the boxplot in Figure 5c. Thinner films consistently show a stronger response; this is expected given that a higher surface area to volume ratio leads to a larger concentration of surface

https://doi.org/10.1021/acsanm.2c01614
ACS Appl. Nano Mater. 2022, 5, 7549−7561

charge carriers reactive to the influence of adsorbed NO_2 molecules compared to the bulk charge carrier concentration, resulting in a greater change in conductivity. While the variance of the devices with a 2.4 nm thick film indicates that other material properties influence sensitivity, it is clear that film thickness is the most important factor.

For the thinnest (2.4 nm) film, a total of eight devices were created, each under different annealing conditions. The effects of each Raman parameter on sensor response are shown in Figure 5d where the $\Delta R/R$ of each device is plotted as a function of each Raman parameter. The results are summarized in a bar plot of the Pearson correlation coefficient (the ratio between the covariance and the product of the standard deviations) in Figure 5e. When comparing the Raman parameters of these devices, the I_A/I_E ratio from the cross-polarized Raman spectra showed the strongest correlation with sensor response. As this ratio corresponds to the orientation of crystal grains, this suggests that OoPO grains tend to result in a greater change in device conductivity, consistent with the results reported by Cho et al.[24] The effects of the Raman parameters are further illustrated in Figure 5e, where the sensor response is plotted for each device alongside a histogram representing the deviation of each variable from its mean value (dashed grey lines in Figure 5d,f). Bars with negative deviation correspond to devices in which the associated Raman parameter fell below the mean value depicted by the dashed grey line in the corresponding plot in Figure 5d. Similarly, bars with positive deviation correspond to devices in which the associated Raman parameter fell above the mean value. In addition to the I_A/I_E ratio, correlations with the E_{2g} linewidth and strain are also present to a lesser extent, which is to be expected as these variables correlate with the I_A/I_E ratio itself, as discussed earlier. However, it is also possible that strain directly influences sensor response—further studies would be needed to distinguish between the effects of strain and grain orientation. Lastly, it is interesting to note that no clear correlation with the I_{LA}/I_E ratio is seen, suggesting that the presence of defects does not play a significant role in sensor response relative to the other variables for the range of defect densities measured here. This is likely due to the rapid termination of highly reactive surface sites by ambient species such as oxygen.

While the laser crystallization process is a versatile high-throughput tool to explore relationships in 2D materials, it is important to note that the optimized device performance demonstrated in this study is very comparable to other 2D chemical sensor devices fabricated by more conventional synthesis strategies. The optimized sensor response to 1 ppm NO_2 resulted in a $\Delta R/R$ of 0.133 (or a response of 13.3%), which is on the order of single-crystal MoS_2 grown by chemical vapor transport under the same conditions tested here and without photoexcitation.[67] Moreover, the response matches high performing atomically thin NO_2 sensors made of $Re_{0.5}Nb_{0.5}S_2$, a novel TMD, which shows a monolayer response of 30% and 6 layer response of 13% to the same concentration of NO_2.[68] Recent advances in pathogen sensing reveal that the laser crystallized few-layer MoS_2 can also detect antigens from Influenza A and SARS-COV-2 at concentrations below pg/mL in relevant saliva solutions.[69] The fact that these sensors can be fabricated simply, cheaply, and completely customized, while maintaining the overall substrate at room temperature makes the proposed methodology very attractive for commercial scale-up and practical applications.

CONCLUSIONS

In order to create tailored devices built around 2D materials, strategies that enable high-throughput, data-driven design will become increasingly important. In this work, a laser-crystallization strategy was used to create hundreds of annealed regions on various samples that reveal unique structure/property relationships. This enabled a high-throughput analysis that resulted in four key advances:

1. After accounting for the effects of film thickness on the A_{1g} and E_{2g} Raman modes for MoS_2, a linear relationship between strain and doping was found through non-resonant Raman analysis of thousands of Raman spectra. Subsequent resonant Raman and XPS analysis revealed that this is an indirect relationship due to the laser-processing conditions, with higher annealing temperatures resulting in two simultaneous effects. First, a reduction in strain is observed due to the formation of larger OoPO grains. Second, a reduction in p-doping due to the incorporation of extant oxygen dopants into MoO_2 bonds is observed.
2. The large library of spectroscopic data enabled the use of a UMAP data visualization approach, revealing clustering based on I_A/I_E values and prompting further investigation. To quantitatively evaluate this ratio, polarized Raman was employed to explore the role of orientation on the strain, doping, and crystal size in laser-annealed MoS_2 films.
3. The large data set enabled the determination of not only correlations between parameters, but also allowed for parameter constraints that were used to provide strong evidence for causal relationships or lack thereof. This analysis revealed the following:
    a. While there is a clear linear dependence upon the linewidth of in-plane and out-of-plane vibrational modes, changes in strain and doping do not cause the observed saturation in A_{1g} linewidth. Instead, a limitation in the amount of transverse disorder based on the film thickness is proposed.
    b. The amount of strain is found to be correlated with both the grain orientation and grain size. However, by keeping confounding variables relatively fixed by constraining the data set, strong evidence of a causal link was established.
4. The ability to induce high-throughput, specific, controllable intrinsic properties at this scale was used to fabricate large-scale conductometric chemical sensors from laser-crystallized MoS_2 regions on substrates with patterned metal contacts. As grain orientation was found to be a highly variable parameter in the Raman analysis, polarized Raman was also used to qualitatively gauge it for the sensor devices, revealing that grain orientation has a strong influence on sensor response in addition to film thickness.

In addition, optical and electronic properties of the laser-crystallized MoS_2 thin films were compared to the repository of resonant and nonresonant Raman spectra, revealing an increase in band gap with greater p-doping. Collectively, the results of this study demonstrate how high-throughput data generation of 2D material processing conditions can accelerate the discovery of material processing mechanisms, as well as the optimization of functional devices such as NO_2 gas sensors. For example, recreating this data set using conventional

https://doi.org/10.1021/acsanm.2c01614
ACS Appl. Nano Mater. 2022, 5, 7549−7561

chemical vapor deposition methods would have increased the timeline of this study by a factor of ∼1000 (assuming ∼1 h versus ∼1 s per processing candidate). Affordable generation of 2D material processing training data sets that will also empower the development of machine learning surrogate models for integration into the fabrication workflow.[70] Using convolutional neural networks or other neural network techniques, optical images of the laser-annealed film can potentially be mapped to material-level or device-level performance characteristics. This mapping will not only accelerate the calibration of processing conditions during early-stage material development but could also serve as a rapid assessment tool for quality control during large-scale production. High-throughput, data-driven design strategies are an important tool for stimulating these opportunities for the 2D materials community.

METHODS

Magnetron Sputtering. The samples consisted of films of a-MoS_2 with varying thicknesses grown on 0.5 mm thick willow glass substrates by magnetron sputtering at a substrate temperature of 25 °C. Sputtering was performed via asymmetric bipolar pulsed direct current magnetron sputtering at 65 kHz (with a 0.4 s reverse time) from a polycrystalline MoS_2 target (Plasmaterials) at room temperature with a growth rate of approximately 1 atomic layer every 4 s. Growth times of 12, 15, 18, 24, 30, and 36 s were used to produce films with thicknesses of 2.4, 3.2, 3.6, 4.9, 6.5, and 7.8 nm, respectively.

Laser Processing. The laser processing setup used is identical to that described by Austin et al.[45] but with a 100× magnification, infinity-corrected objective lens (Mitutoyo N02027112) with a numerical aperture of 0.55. The $1/e^2$ beam radius during processing was measured to be 10.0 ± 0.2 μm. Each sample was placed in an environmental gas cell and brought to a rough vacuum (30 mTorr) before 99.999% purity argon gas was flowed into the cell with an equilibrium pressure of 11 Torr before laser-processing. Each laser-written region was formed by raster-scanning the laser eight times with a separation of 6 μm between each raster and with a length of 1 mm.

Raman Spectroscopy. The Raman spectra were obtained using a Renishaw InVia with 1800 and 1200 lines/mm gratings for the 514.5 and 633 nm excitation lasers, respectively. A 100× objective lens with a numerical aperture of 0.85 was used, resulting in a spatial resolution of 1 μm. The laser power was kept below 1 mW to minimize any heating by the laser. Spectra were collected from unannealed a-MoS_2 and select laser-crystallized 2H-MoS_2 regions over the course of 10 consecutive 30 s acquisitions with 2 accumulations each.

TEM Specimen Preparation and Electron Microscopy. The TEM specimens of the films were prepared via a focused ion beam (FIB) milling process employing a Helios Nano Lab 660 FIB unit. STEM images were recorded on a Nion UltraSTEM 100 operating at 100 kV, with a convergence angle of 32 mrad. The HAADF detector possessed an inner collection angle of ∼80 mrad and an outer collection angle of ∼200 mrad. The STEM was equipped with a Gatan Enfina electron energy-loss (EEL) spectrometer and the EELS experiments were performed with a convergence semi-angle of 30 mrad, and an EELS collection semi-angle of 48 mrad.

Ultraviolet−visible Spectroscopy. Absorption spectra were collected using a CRAIC UV−vis microspectrophotometer via transmission using a 15× objective over a wavelength range of 300−1600 nm. Effects of dark current and the substrate were accounted for by taking a dark scan and a reference scan of the substrate.

Conductivity Measurements. In order to perform conductivity measurements, resistors were fabricated using two e-beam lithography steps. In both steps, the glass substrate was spin-coated with MMA and PMMA photoresist stacks. To avoid charging effects associated with glass (insulating) substrate, 20 nm of Au is deposited on top of the MMA/PMMA stack. Following that, e-beam lithography was used to expose the desired regions. After exposure, Au was removed using trifluoroacetic acid and the exposed regions were developed using MIBK and IPA. In the first step, the MoS_2 channel was defined, and MoS_2 was etched from the rest of the sample using SF6. In the second step, e-beam evaporation was performed to deposit a 40 nm Ni/30 nm Au stack. Finally, the photoresist is removed using acetone and IPA in both cases. Conductivity measurements were performed using a Keysight B1500A parameter analyzer inside a Lake Shore CRX-VF probe station at room temperature in a high vacuum (∼10^{-6} Torr).

Sensor Testing. Sensing was tested in a homebuilt 2.2 L stainless steel chamber. The sample was placed inside and flushed overnight with dry oxygen. Patterned contacts were deposited first onto the wafers followed by amorphous MoS_2 deposition and subsequent laser annealing. The contacts used in this study were 10 nm Ti/100 nm Au deposited by e-beam evaporation. The contact resistance is expected to play a minimal role in the device performance as the sensors consider relative responses, so no postdeposition thermal annealing was performed. Resistance measurements were taken with a Keysight DAQ970A containing a DAQM900A 20-channel solid-state multiplexer module at 6.5 digits of precision integrating over 10 power line cycles with a connection fed through a 37-pin subminiature-D CF flange (Kurt Lesker). 10 ppm NO_2 balanced with nitrogen (Indiana Oxygen) was mixed with dry nitrogen using mass flow controllers (MKS Instruments 1179C series) to produce the desired concentration (1:9 for 1 ppm). The total flow was held at 2000 sccm.

ASSOCIATED CONTENT

Supporting Information

The Supporting Information is available free of charge at https://pubs.acs.org/doi/10.1021/acsanm.2c01614.

Full-size microscope and STEM images, more detailed description of the Raman spectra analysis, and additional plots of variables derived from the Raman spectra (PDF)

AUTHOR INFORMATION

Corresponding Authors

Christopher Muratore − *Department of Chemical and Materials Engineering, University of Dayton, Dayton, Ohio 45469, United States;* orcid.org/0000-0002-5555-9261; Email: cmuratore1@udayton.edu

Nicholas R. Glavin − *Materials and Manufacturing Directorate, Air Force Research Laboratory, Wright-Patterson AFB, Ohio 45433, United States;* orcid.org/0000-0002-9447-7509; Email: nicholas.glavin.1@us.af.mil

Authors

Drake Austin − *Materials and Manufacturing Directorate, Air Force Research Laboratory, Wright-Patterson AFB, Ohio 45433, United States; UES Inc., Dayton, Ohio 45432, United States*

Paige Miesle − *Materials and Manufacturing Directorate, Air Force Research Laboratory, Wright-Patterson AFB, Ohio 45433, United States; UES Inc., Dayton, Ohio 45432, United States; Department of Chemical and Materials Engineering, University of Dayton, Dayton, Ohio 45469, United States*

Deanna Sessions − *Materials and Manufacturing Directorate, Air Force Research Laboratory, Wright-Patterson AFB, Ohio 45433, United States; UES Inc., Dayton, Ohio 45432, United States; Department of Electrical Engineering, Pennsylvania State University, University Park, Pennsylvania 16802, United States*

Michael Motala − *Materials and Manufacturing Directorate, Air Force Research Laboratory, Wright-Patterson AFB, Ohio*

https://doi.org/10.1021/acsanm.2c01614
ACS Appl. Nano Mater. 2022, 5, 7549−7561

45433, United States; UES Inc., Dayton, Ohio 45432, United States

David C. Moore − *Materials and Manufacturing Directorate, Air Force Research Laboratory, Wright-Patterson AFB, Ohio 45433, United States; UES Inc., Dayton, Ohio 45432, United States*

Griffin Beyer − *Materials and Manufacturing Directorate, Air Force Research Laboratory, Wright-Patterson AFB, Ohio 45433, United States; UES Inc., Dayton, Ohio 45432, United States; Department of Chemical and Materials Engineering, University of Dayton, Dayton, Ohio 45469, United States*

Adam Miesle − *Materials and Manufacturing Directorate, Air Force Research Laboratory, Wright-Patterson AFB, Ohio 45433, United States; UES Inc., Dayton, Ohio 45432, United States; Department of Chemical and Materials Engineering, University of Dayton, Dayton, Ohio 45469, United States*

Andrew Sarangan − *Department of Chemical and Materials Engineering, University of Dayton, Dayton, Ohio 45469, United States*

Amritanand Sebastian − *Department of Engineering Science and Mechanics, Pennsylvania State University, University Park, Pennsylvania 16802, United States*

Saptarshi Das − *Department of Engineering Science and Mechanics and Department of Materials Science and Engineering, Pennsylvania State University, University Park, Pennsylvania 16802, United States;* orcid.org/0000-0002-0188-945X

Anand B. Puthirath − *Department of Materials Science and NanoEngineering, Rice University, Houston, Texas 77005, United States*

Xiang Zhang − *Center for Nanophase Materials Science, Oak Ridge National Laboratory, Oak Ridge, Tennessee 37831, United States;* orcid.org/0000-0003-4004-5185

Jordan Hachtel − *Center for Nanophase Materials Science, Oak Ridge National Laboratory, Oak Ridge, Tennessee 37831, United States*

Pulickel M. Ajayan − *Department of Materials Science and NanoEngineering, Rice University, Houston, Texas 77005, United States;* orcid.org/0000-0001-8323-7860

Tyson Back − *Materials and Manufacturing Directorate, Air Force Research Laboratory, Wright-Patterson AFB, Ohio 45433, United States*

Peter R. Stevenson − *Materials and Manufacturing Directorate, Air Force Research Laboratory, Wright-Patterson AFB, Ohio 45433, United States;* orcid.org/0000-0003-3731-1630

Michael Brothers − *UES Inc., Dayton, Ohio 45432, United States; Air Force Research Laboratory, Wright-Patterson AFB, Ohio 45433, United States;* orcid.org/0000-0002-8239-2399

Steve S. Kim − *Air Force Research Laboratory, Wright-Patterson AFB, Ohio 45433, United States;* orcid.org/0000-0002-9519-077X

Philip Buskohl − *Materials and Manufacturing Directorate, Air Force Research Laboratory, Wright-Patterson AFB, Ohio 45433, United States*

Rahul Rao − *Materials and Manufacturing Directorate, Air Force Research Laboratory, Wright-Patterson AFB, Ohio 45433, United States*

Complete contact information is available at: https://pubs.acs.org/10.1021/acsanm.2c01614

Notes

The authors declare no competing financial interest.

■ ACKNOWLEDGMENTS

N.G., D.A., and P.M. acknowledge support from the Asian Office of Aerospace Research and Development within the Air Force Office of Scientific Research grant #21IOA110 as well as support from the Air Force Office of Scientific Research under grant number 20RXCOR057. S. K. and G.B. acknowledge support from the DAGSI fellowship. A.B.P. and P.M.A. gratefully acknowledge the financial support from the National Science Foundation through the I/UCRC Center for Atomically Thin Multifunctional Coatings. STEM experiments were conducted as part of a user proposal at the Center for Nanophase Materials Sciences, which is a DOE Office of Science User Facility.

■ REFERENCES

(1) Mehmood, F.; Pachter, R.; Back, T. C.; Boeckl, J. J.; Busch, R. T.; Stevenson, P. R. Two-dimensional MoS_2 2H, 1T, and 1T′ crystalline phases with incorporated adatoms: theoretical investigation of electronic and optical properties. *Appl. Opt.* **2021**, *60*, G232−G242.

(2) Ayari, A.; Cobas, E.; Ogundadegbe, O.; Fuhrer, M. S. Realization and electrical characterization of ultrathin crystals of layered transition-metal dichalcogenides. *J. Appl. Phys.* **2007**, *101*, 014507.

(3) Soluyanov, A. A.; Gresch, D.; Wang, Z.; Wu, Q.; Troyer, M.; Dai, X.; Bernevig, B. A. Type-II Weyl semimetals. *Nature* **2015**, *527*, 495−498.

(4) Wang, Q. H. Electronics and optoelectronics of two-dimensional transition metal dichalcogenides. *Nat. Nanotechnol.* **2012**, *7*, 699.

(5) Chakraborty, B.; Matte, H. S. S. R.; Sood, A. K.; Rao, C. N. R. Layer-dependent resonant Raman scattering of a few layer MoS_2: Raman scattering of a few layer MoS_2. *J. Raman Spectrosc.* **2013**, *44*, 92−96.

(6) Liang, L.; Meunier, V. First-Principles Raman Spectra of MoS_2, WS_2 and Their Heterostructures. *Nanoscale* **2014**, *6*, 5394.

(7) Lee, C.; Yan, H.; Brus, L. E.; Heinz, T. F.; Hone, J.; Ryu, S. Anomalous Lattice Vibrations of Single- and Few-Layer MoS_2. *ACS Nano* **2010**, *4*, 2695−2700.

(8) Wang, Y.; Cong, C.; Qiu, C.; Yu, T. Raman Spectroscopy Study of Lattice Vibration and Crystallographic Orientation of Monolayer MoS_2 under Uniaxial Strain. *Small* **2013**, *9*, 2857−2861.

(9) Rice, C.; Young, R. J.; Zan, R.; Bangert, U.; Wolverson, D.; Georgiou, T.; Jalil, R.; Novoselov, K. S. Raman-Scattering Measurements and First-Principles Calculations of Strain-Induced Phonon Shifts in Monolayer MoS_2. *Phys. Rev. B: Condens. Matter Mater. Phys.* **2013**, *87*, 081307.

(10) Huang, Y. L.; Chen, Y.; Zhang, W.; Quek, S. Y.; Chen, C.-H.; Li, L.-J.; Hsu, W.-T.; Chang, W.-H.; Zheng, Y. J.; Chen, W.; Wee, A. T. S. Bandgap Tunability at Single-Layer Molybdenum Disulphide Grain Boundaries. *Nat. Commun.* **2015**, *6*, 6298.

(11) Castellanos-Gomez, A.; Roldán, R.; Cappelluti, E.; Buscema, M.; Guinea, F.; van der Zant, H. S. J.; Steele, G. A. Local Strain Engineering in Atomically Thin MoS_2. *Nano Lett.* **2013**, *13*, 5361−5366.

(12) Zhou, M.; Wang, W.; Lu, J.; Ni, Z. How Defects Influence the Photoluminescence of TMDCs. *Nano Res.* **2021**, *14*, 29−39.

(13) Fujisawa, K.; Carvalho, B. R.; Zhang, T.; Perea-López, N.; Lin, Z.; Carozo, V.; Ramos, S. L. L. M.; Kahn, E.; Bolotsky, A.; Liu, H.; Elías, A. L.; Terrones, M. Quantification and Healing of Defects in Atomically Thin Molybdenum Disulfide: Beyond the Controlled Creation of Atomic Defects. *ACS Nano* **2021**, *15*, 9658−9669.

(14) Chow, P. K.; Jacobs-Gedrim, R. B.; Gao, J.; Lu, T.-M.; Yu, B.; Terrones, H.; Koratkar, N. Defect-Induced Photoluminescence in

Monolayer Semiconducting Transition Metal Dichalcogenides. *ACS Nano* **2015**, *9*, 1520−1527.
(15) Lin, Z.; Carvalho, B. R.; Kahn, E.; Lv, R.; Rao, R.; Terrones, H.; Pimenta, M. A.; Terrones, M. Defect Engineering of Two-Dimensional Transition Metal Dichalcogenides. *2D Mater.* **2016**, *3*, 022002.
(16) Stevenson, P. R.; Busch, R. T.; Torsi, R.; Jawaid, A. M.; Rao, R.; Lioi, D. B.; Robinson, J. A.; Glavin, N. R.; Vaia, R. A.; Kennedy, W. J.; Vernon, J. P. Reversibly Tailoring Optical Constants of Monolayer Transition Metal Dichalcogenide MoS_2 Films: Impact of Dopant-Induced Screening from Chemical Adsorbates and Mild Film Degradation. *ACS Photonics* **2021**, *8*, 1705−1717.
(17) Moore, D. C.; Jawaid, A.; Busch, R.; Brothers, M.; Miesle, P.; Miesle, A.; Rao, R.; Lee, J.; Beagle, L. K.; Motala, M.; Wallace, S. G.; Downing, J. R.; Roy, A.; Muratore, C.; Hersam, M. C.; Vaia, R.; Kim, S.; Glavin, N. R. Ultrasensitive molecular sensors based on real-time impedance spectroscopy in solution-processed 2d materials. *Adv. Funct. Mater.* **2021**, *32*, 2106830.
(18) Motala, M.; Beagle, L. K.; Lynch, J.; Moore, D. C.; Stevenson, P. R.; Benton, A.; Tran, L. D.; Baldwin, L. A.; Austin, D.; Muratore, C.; Jariwala, D.; Glavin, N. R. Selective vapor sensors with thin-film MoS_2-coated optical fibers. *J. Vac. Sci. Technol., A* **2022**, *40*, 032202.
(19) Cho, B.; Hahm, M. G.; Choi, M.; Yoon, J.; Kim, A. R.; Lee, Y.-J.; Park, S.-G.; Kwon, J.-D.; Kim, C. S.; Song, M.; Jeong, Y.; Nam, K.-S.; Lee, S.; Yoo, T. J.; Kang, C. G.; Lee, B. H.; Ko, H. C.; Ajayan, P. M.; Kim, D.-H. Charge-transfer-based Gas Sensing Using Atomic-layer MoS_2. *Sci. Rep.* **2015**, *5*, 8052.
(20) Potyrailo, R. A.; Mirsky, V. M. Combinatorial and High-Throughput Development of Sensing Materials: The First 10 Years. *Chem. Rev.* **2008**, *108*, 770−813.
(21) Late, D. J.; Huang, Y.-K.; Liu, B.; Acharya, J.; Shirodkar, S. N.; Luo, J.; Yan, A.; Charles, D.; Waghmare, U. V.; Dravid, V. P.; Rao, C. N. R. Sensing Behavior of Atomically Thin-Layered MoS_2 Transistors. *ACS Nano* **2013**, *7*, 4879−4891.
(22) González, C.; Biel, B.; Dappe, Y. J. Adsorption of Small Inorganic Molecules on a Defective MoS_2 Monolayer. *Phys. Chem. Chem. Phys.* **2017**, *19*, 9485−9499.
(23) Yu, N.; Wang, L.; Li, M.; Sun, X.; Hou, T.; Li, Y. Molybdenum Disulfide as a Highly Efficient Absorbent for Non-polar Gases. *Phys. Chem. Chem. Phys.* **2015**, *17*, 11700−11704.
(24) Cho, S.-Y.; Kim, S. J.; Lee, Y.; Kim, J.-S.; Jung, W.-B.; Yoo, H.-W.; Kim, J.; Jung, H.-T. Highly Enhanced Gas Adsorption Properties in Vertically Aligned MoS_2 Layers. *ACS Nano* **2015**, *9*, 9314−9321.
(25) Kumar, R. R.; Habib, M. R.; Khan, A.; Chen, P.-C.; Murugesan, T.; Gupta, S.; Anbalagan, A. k.; Tai, N.-H.; Lee, C.-H.; Lin, H.-N. Sulfur Monovacancies in Liquid-Exfoliated MoS_2 Nanosheets for NO_2 Gas Sensing. *ACS Appl. Nano Mater.* **2021**, *4*, 9459−9470.
(26) Li, F.; Shi, C. NO-Sensing Performance of Vacancy Defective Monolayer MoS2 Predicted by Density Function Theory. *Appl. Surf. Sci.* **2018**, *434*, 294−306.
(27) Zavabeti, A.; Jannat, A.; Zhong, L.; Haidry, A. A.; Yao, Z.; Ou, J. Z. Two-Dimensional Materials in Large-Areas: Synthesis, Properties and Applications. *Nano-Micro Lett.* **2020**, *12*, 66.
(28) Cai, Z.; Liu, B.; Zou, X.; Cheng, H.-M. Chemical Vapor Deposition Growth and Applications of Two-Dimensional Materials and Their Heterostructures. *Chem. Rev.* **2018**, *118*, 6091−6133.
(29) Muratore, C.; Voevodin, A. A.; Glavin, N. R. Physical Vapor Deposition of 2D Van Der Waals Materials: A Review. *Thin Solid Films* **2019**, *688*, 137500.
(30) Kim, R. H.; Leem, J.; Muratore, C.; Nam, S.; Rao, R.; Jawaid, A.; Durstock, M.; McConney, M.; Drummy, L.; Rai, R.; Voevodin, A.; Glavin, N. Photonic Crystallization of Two-Dimensional MoS_2 for Stretchable Photodetectors. *Nanoscale* **2019**, *11*, 13260−13268.
(31) Bizhani, M.; Thorat, R.; Poston, W.; Wickramasinghe, T.; Aleithan, S. H.; Stinaff, E. Thermal Annealing Effects on Naturally Contacted Monolayer MoS_2. *Phys. Status Solidi B* **2021**, *258*, 2000426.
(32) Michail, A.; Delikoukos, N.; Parthenios, J.; Galiotis, C.; Papagelis, K. Optical Detection of Strain and Doping Inhomogeneities in Single Layer MoS_2. *Appl. Phys. Lett.* **2016**, *108*, 173102.
(33) Abbas, O. A.; Lewis, A. H.; Aspiotis, N.; Huang, C.-C.; Zeimpekis, I.; Hewak, D. W.; Sazio, P.; Mailis, S. Laser Printed Two-Dimensional Transition Metal Dichalcogenides. *Sci. Rep.* **2021**, *11*, 5211.
(34) Huang, C.-C.; Medina, H.; Chen, Y.-Z.; Su, T.-Y.; Li, J.-G.; Chen, C.-W.; Yen, Y.-T.; Wang, Z. M.; Chueh, Y.-L. Transfer-Free Growth of Atomically Thin Transition Metal Disulfides Using a Solution Precursor by a Laser Irradiation Process and Their Application in Low-Power Photodetectors. *Nano Lett.* **2016**, *16*, 2463−2470.
(35) Heyne, M. H.; de Marneffe, J.-F.; Radu, I.; Neyts, E. C.; De Gendt, S. Thermal Recrystallization of Short-Range Ordered WS_2 Films. *J. Vac. Sci. Technol., A* **2018**, *36*, 05G501.
(36) Wuenschell, J. K.; Helvajian, H. Enhanced Laser Crystallization of Thin Film Amorphous Molybdenum Disulfide (MoS_2) by Means of Pulsed Laser Ultrasound. *Opt. Express* **2019**, *27*, 5859.
(37) Sirota, B.; Glavin, N.; Voevodin, A. A. Room Temperature Magnetron Sputtering and Laser Annealing of Ultrathin MoS_2 for Flexible Transistors. *Vacuum* **2019**, *160*, 133−138.
(38) Kim, E.; Ko, C.; Kim, K.; Chen, Y.; Suh, J.; Ryu, S.-G.; Wu, K.; Meng, X.; Suslu, A.; Tongay, S.; Wu, J.; Grigoropoulos, C. P. Site Selective Doping of Ultrathin Metal Dichalcogenides by Laser-Assisted Reaction. *Adv. Mater.* **2016**, *28*, 341−346.
(39) Afaneh, T.; Sahoo, P. K.; Nobrega, I. A. P.; Xin, Y.; Gutiérrez, H. R. Laser-Assisted Chemical Modification of Monolayer Transition Metal Dichalcogenides. *Adv. Funct. Mater.* **2018**, *28*, 1802949.
(40) Lu, J.; Carvalho, A.; Chan, X. K.; Liu, H.; Liu, B.; Tok, E. S.; Loh, K. P.; Castro Neto, A. H.; Sow, C. H. Atomic Healing of Defects in Transition Metal Dichalcogenides. *Nano Lett.* **2015**, *15*, 3524−3532.
(41) Rani, R.; Dimple; Jena, N.; Kundu, A.; Sarkar, A. D.; Hazra, K. S. Controlled Formation of Nanostructures on MoS_2 Layers by Focused Laser Irradiation. *Appl. Phys. Lett.* **2017**, *110*, 083101.
(42) Kim, S. W.; Na, J. H.; Choi, W. L.; Chung, H.-J.; Jhang, S. H.; Choi, S. H.; Yang, W.; Lee, S. W. Patterning of Periodic Ripples in Monolayer MoS_2 by Using Laser Irradiation. *J. Korean. Soc.* **2016**, *69*, 1505−1508.
(43) Alrasheed, A.; Gorham, J. M.; Tran Khac, B. C.; Alsaffar, F.; DelRio, F. W.; Chung, K.-H.; Amer, M. R. Surface Properties of Laser-Treated Molybdenum Disulfide Nanosheets for Optoelectronic Applications. *ACS Appl. Mater. Interfaces* **2018**, *10*, 18104−18112.
(44) Muratore, C.; Hu, J. J.; Wang, B.; Haque, M. A.; Bultman, J. E.; Jespersen, M. L.; Shamberger, P. J.; McConney, M. E.; Naguy, R. D.; Voevodin, A. A. Continuous Ultra-Thin MoS_2 Films Grown by Low-Temperature Physical Vapor Deposition. *Appl. Phys. Lett.* **2014**, *104*, 261604.
(45) Austin, D.; Gliebe, K.; Muratore, C.; Boyer, B.; Fisher, T. S.; Beagle, L. K.; Benton, A.; Look, P.; Moore, D.; Ringe, E.; Treml, B.; Jawaid, A.; Vaia, R.; Joshua Kennedy, W.; Buskohl, P.; Glavin, N. R. Laser Writing of Electronic Circuitry in Thin Film Molybdenum Disulfide: A Transformative Manufacturing Approach. *Mater. Today* **2021**, *43*, 17−26.
(46) Atkin, P.; Lau, D. W. M.; Zhang, Q.; Zheng, C.; Berean, K. J.; Field, M. R.; Ou, J. Z.; Cole, I. S.; Daeneke, T.; Kalantar-Zadeh, K. Laser Exposure Induced Alteration of WS_2 Monolayers in the Presence of Ambient Moisture. *2D Mater.* **2017**, *5*, 015013.
(47) Liu, M.; Shi, J.; Li, Y.; Zhou, X.; Ma, D.; Qi, Y.; Zhang, Y.; Liu, Z. Temperature-Triggered Sulfur Vacancy Evolution in Monolayer MoS_2/Graphene Heterostructures. *Small* **2017**, *13*, 1602967.
(48) Wood, R. M. Laser Induced Damage Thresholds and Laser Safety Levels. Do the Units of Measurement Matter? *Opt. Laser Technol.* **1998**, *29*, 517−522.
(49) Rao, R.; Islam, A. E.; Singh, S.; Berry, R.; Kawakami, R. K.; Maruyama, B.; Katoch, J. Spectroscopic Evaluation of Charge-Transfer Doping and Strain in Graphene/ MoS_2 Heterostructures. *Phys. Rev. B* **2019**, *99*, 195401.
(50) Chakraborty, B.; Bera, A.; Muthu, D. V. S.; Bhowmick, S.; Waghmare, U. V.; Sood, A. K. Symmetry-Dependent Phonon

https://doi.org/10.1021/acsanm.2c01614
ACS Appl. Nano Mater. 2022, 5, 7549−7561

Renormalization in Monolayer MoS_2 Transistor. *Phys. Rev. B: Condens. Matter Mater. Phys.* **2012**, *85*, 161403.
(51) Li, H.; Zhang, Q.; Yap, C. C. R.; Tay, B. K.; Edwin, T. H. T.; Olivier, A.; Baillargeat, D. From Bulk to Monolayer MoS_2: Evolution of Raman Scattering. *Adv. Funct. Mater.* **2012**, *22*, 1385−1390.
(52) Zhang, X.; Qiao, X. F.; Shi, W.; Wu, J. B.; Jiang, D. S.; Tan, P. H. Phonon and Raman Scattering of Two-Dimensional Transition Metal Dichalcogenides from Monolayer, Multilayer to Bulk Material. *Chem. Soc. Rev.* **2015**, *44*, 2757.
(53) McDevitt, N. T.; Zabinski, J. S.; Donley, M. S.; Bultman, J. E. Disorder-Induced Low-Frequency Raman Band Observed in Deposited MoS_2 Films. *Appl. Spectrosc.* **1994**, *48*, 733−736.
(54) Nalin Mehta, A.; Mo, J.; Pourtois, G.; Dabral, A.; Groven, B.; Bender, H.; Favia, P.; Caymax, M.; Vandervorst, W. Grain-Boundary-Induced Strain and Distortion in Epitaxial Bilayer MoS_2 Lattice. *J. Phys. Chem. C* **2020**, *124*, 6472−6478.
(55) Vandalon, V.; Sharma, A.; Perrotta, A.; Schrode, B.; Verheijen, M. A.; Bol, A. A. Polarized Raman Spectroscopy to Elucidate the Texture of Synthesized MoS_2. *Nanoscale* **2019**, *11*, 22860−22870.
(56) McInnes, L.; Healy, J.; Melville, J. UMAP: Uniform Manifold Approximation and Projection for Dimension Reduction. **2020**, arXiv: 1802.03426 [cs, stat].
(57) Pearson, K. On Lines and Planes of Closest Fit to Systems of Points in Space. *London, Edinburgh Dublin Philos. Mag. J. Sci.* **1901**, *2*, 559−572.
(58) Hotelling, H. Analysis of a Complex of Statistical Variables into Principal Components. *J. Educ. Psychol.* **1933**, *24*, 417−441.
(59) Mignuzzi, S.; Pollard, A. J.; Bonini, N.; Brennan, B.; Gilmore, I. S.; Pimenta, M. A.; Richards, D.; Roy, D. Effect of Disorder on Raman Scattering of Single-Layer MoS_2. *Phys. Rev. B: Condens. Matter Mater. Phys.* **2015**, *91*, 195411.
(60) Rao, R.; Islam, A. E.; Campbell, P. M.; Vogel, E. M.; Maruyama, B. In Situ Thermal Oxidation Kinetics in Few Layer MoS_2. *2D Mater.* **2017**, *4*, 025058.
(61) Gillen, R.; Maultzsch, J. Light-Matter Interactions in Two-Dimensional Transition Metal Dichalcogenides: Dominant Excitonic Transitions in Mono- and Few-Layer MoX_2 and Band Nesting. *IEEE J. Sel. Top. Quantum Electron.* **2017**, *23*, 219−230.
(62) Wendumu, T. B.; Seifert, G.; Lorenz, T.; Joswig, J.-O.; Enyashin, A. Optical Properties of Triangular Molybdenum Disulfide Nanoflakes. *J. Phys. Chem. Lett.* **2014**, *5*, 3636−3640.
(63) Wilcoxon, J. P.; Samara, G. A. Strong Quantum-Size Effects in a Layered Semiconductor: MoS_2 Nanoclusters. *Phys. Rev. B: Condens. Matter Mater. Phys.* **1995**, *51*, 7299−7302.
(64) Rao, R.; Carozo, V.; Wang, Y.; Islam, A. E.; Perea-Lopez, N.; Fujisawa, K.; Crespi, V. H.; Terrones, M.; Maruyama, B. Dynamics of Cleaning, Passivating and Doping Monolayer MoS_2 by Controlled Laser Irradiation. *2D Mater.* **2019**, *6*, 045031.
(65) Lee, C. W.; Suh, J. M.; Jang, H. W. Chemical Sensors Based on Two-Dimensional (2D) Materials for Selective Detection of Ions and Molecules in Liquid. *Front. Chem* **2019**, *7*, 708.
(66) Meng, Z.; Stolz, R. M.; Mendecki, L.; Mirica, K. A. Electrically-Transduced Chemical Sensors Based on Two-Dimensional Nanomaterials. *Chem. Rev.* **2019**, *119*, 478−598.
(67) Zheng, W.; Xu, Y.; Zheng, L.; Yang, C.; Pinna, N.; Liu, X.; Zhang, J. MoS_2 Van der Waals p−n Junctions Enabling Highly Selective Room-Temperature NO_2 Sensor. *Adv. Funct. Mater.* **2020**, *30*, 2000435.
(68) Azizi, A.; Dogan, M.; Long, H.; Cain, J. D.; Lee, K.; Eskandari, R.; Varieschi, A.; Glazer, E. C.; Cohen, M. L.; Zettl, A. High-Performance Atomically-Thin Room-Temperature NO_2 Sensor. *Nano Lett.* **2020**, *20*, 6120−6127.
(69) Muratore, C.; Muratore, M. K.; Austin, D. R.; Miesle, P.; Benton, A. K.; Beagle, L. K.; Motala, M. J.; Moore, D. C.; Slocik, J. M.; Brothers, M.; Kim, S. S.; Krupa, K.; Back, T. A.; Grant, J. T.; Glavin, N. R. Laser-Fabricated 2D Molybdenum Disulfide Electronic Sensor Arrays for Rapid, Low-Cost Ultrasensitive Detection of Influenza A and SARS-COV-2. *Adv. Mater. Interfac.* **2022**, 2102209.
(70) Sessions, D.; Meenakshisundaram, V.; Gillman, A.; Cook, A.; Fuchi, K.; Buskohl, P. R.; Huff, G. H. Mapping Geometric and Electromagnetic Feature Spaces with Machine Learning for Additively Manufactured RF Devices. *Addit. Manuf.* **2022**, *50*, 102549.

https://doi.org/10.1021/acsanm.2c01614
ACS Appl. Nano Mater. 2022, 5, 7549−7561